POLITECNICO
MILANO 1863

SCUOLA DI INGEGNERIA INDUSTRIALE
E DELL'INFORMAZIONE

Executive Summary of the Thesis

Synthetic Thermal Image Generation Towards Enhanced Close-Proximity Navigation in Space

Laurea Magistrale in Space Engineering - Ingegneria Spaziale

Author: Lucia Bianchi

Advisor: Prof. Michèle Roberta Lavagna

Co-advisor: Michele Bechini, Matteo Quirino

Academic year: 2022-2023

1. Introduction

The new scenarios foreseen in forthcoming space missions have increased interests towards optical navigation for relative maneuvers, which have demonstrated efficacy in a variety of operational conditions around cooperative or uncooperative targets. In this context, the necessity for robust real-time guidance, navigation and control procedures is emphasized to ensure successful services and guarantee a correct interaction between objects in space.
With a shift towards autonomous on-board operations, the capability of the Chaser spacecraft to reconstruct the surrounding scene and determine its relative position with respect to the mission Target becomes essential. To accomplish this, monocular Visible (VIS) cameras have found widespread application in close-range mission scenarios, as lightweight and power-effective sensors. However, they struggle in weak lighting conditions, strongly impacting on the overall robustness and accuracy of measurements. A promising solution proposed in literature involves the use of multi-spectral imaging, which combines visible and thermal bands to generate hybrid images; yet, current research relies on synthetic images with stringent assumptions and deep-space backgrounds. Consequently, this thesis proposes an innovative and flexible rendering workflow designed to generate physically accurate Thermal Infrared (TIR) images representative of close-proximity scenarios, where the Earth is introduced into the scene and noises are integrated in the final representation. The synthetic images are then used to evaluate State of The Art (SoTA) object detection and feature extraction algorithms, aiming to investigate the potential benefits of using thermal imaging as a standalone modality for space navigation.

2. Literature review

TIR imaging As of today, no in-flight thermal images of artificial targets are currently available, and only few examples of synthetic representations can be found in literature. A VIS-TIR collection of images is proposed in [1], which includes synthetic representations of space debris with the Earth in the background. Even though this data-set is open-source, it does not provide a sufficiently large volume of raw data. Consequently, to generate synthetic TIR images, image processing techniques might be employed, converting visible images into thermal one via traditional or machine learning algo-

rithms. Yet, the final result lacks intrinsic thermal information and fails to completely remove some of the optical features proper of the VIS imagery.

Earth infrared model To introduce the Earth into the final scene representations, images captured by the Himawari satellite may be exploited, although they lack of radiometric information. Rather than implementing an entire analytical framework, [2] proposes an ESA-developed tool which exploits Clouds and Earth's Radiant Energy System (CERES) database [3] to compute the Top Of Atmosphere (TOA) Earth fluxes.

3. Thermal Infrared Sensor

To enhance the realism of the final image, the model of a thermal sensor is implemented. Assuming the Target spacecraft behaves as a diffuse gray-body with emissivity ε and temperature T, its emitted radiation field is computed through the generalized Boltzmann equation. Yet, the radiation reaching the detector element of the sensor is influenced by the optical elements of the camera; thus, it is expressed as [4]:

$$q_{det} = F_{Target \to det}\ \pi \int_0^\infty \varepsilon B_\lambda(T,\lambda) R(\lambda) d\lambda \quad (1)$$

Where $F_{Trg \to det}$ is the view factor, B_λ is the monochromatic radiation according to Planck's law, and $R(\lambda)$ is the camera response function, dependent upon camera detection efficiency, lens transparency and band-pass filter transmittance.

3.1. Sensor's modes

The use of thermal sensors in space-related applications is twofold: detecting the Target at an unknown distance, and acquiring radiometric data.

Radiometry mode For missions requiring the thermal characterization of the Target, the digital output of the sensor can be expressed as:

$$S = A + B q_{Target} + Noise_{ADU} \quad (2)$$

Here, $Noise_{ADU}$ is the 2D noise distribution, and A and B are the camera calibration parameters. The emitted radiation field of the Target q_{Target} is reconstructed from the radiation reaching the detector element by introducing two compensating factors:

$$q_{Target} = \mathcal{D}\ \mathcal{O}(T)\ q_{det} \quad (3)$$

Here $\mathcal{D}$ is the distance compensation coefficient used to simulate the virtual alignment to the calibration set-up, and $\mathcal{O}(T)$ is the optics compensation factor, dependent upon the scene temperature.
Once the raw camera output is obtained, the radiative temperature field of the observed scene is recovered using Eq.(2):

$$T_{rad,\ Trg} = \sqrt[4]{\frac{S-A}{\sigma B}} \quad (4)$$

Detection mode Assuming the primary objective of the Chaser is exclusively to detect the presence of the Target, no compensation factors are considered. Hence, the final raw output of the thermal camera is given by:

$$S = A + B q_{det} + Noise_{ADU} \quad (5)$$

Where q_{det} is derived from Eq.(1).

3.2. Noise sources

In the context of an uncooled microbolometer array, the main sources of disturbance are Johnson noise, Flicker noise, and temperature fluctuation noise [5]. Upon implementing an electric circuit model, the Root Mean Square (RMS) noise voltages are computed and the resulting values are summarized in Table 1.

Table 1: RMS noise voltages.

v_J	$v_{1/f}$	v_{th}
5.39×10^{-6}	5.32×10^{-6}	2.62×10^{-6}

Among these sources, Flicker is the dominant noise at lower frequencies, being inversely proportional to the frequency; instead, at higher frequencies, the sensor's performance is influenced by Johnson and temperature fluctuation noises. Between these latter disturbances, Johnson is the predominant one, as it is closely tied to the sensing material's temperature. Indeed, due to the absence of a cooling system, the elevated

detector temperature reduces its capability to accurately measure weak infrared signals.
By looking at cumulative Noise Voltage Density (NVD) in Figure 1, given by the sum of all the RMS voltage contributions divided by the frequency bandwidth, it can be observed how after the low frequency range, it reaches a steady value corresponding to the combined effect of Johnson and temperature fluctuation noises.

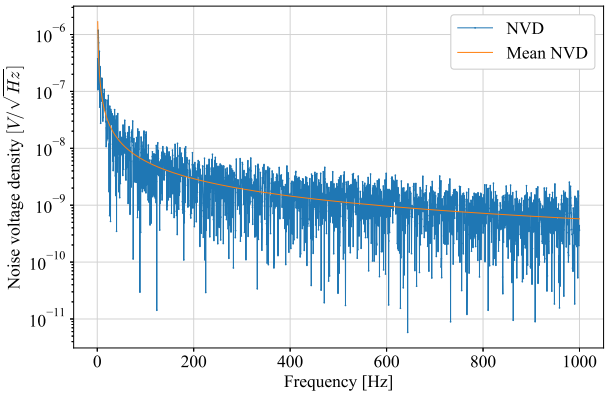

Figure 1: Cumulative noise voltage density of the generic pixel p of the detector.

To preserve the flexibility of the pipeline, the noise distribution is converted into a 2D map that is added to the image during post-processing operations. Hence, starting from Gaussian distributions with appropriate standard deviations, the noise voltages are converted into ADU units through an Analog to Digital (A/D) converter gain, set as $G_{A/D}$ =2470 ADU V^{-1}.

4. TIR image rendering

The absence of in-flight thermal images of a spacecraft imposes the need for generating a synthetic data-set using a suitable rendering tool. The proposed rendering pipeline, reported in Figure 4, ensures a degree of flexibility by individually and concurrently characterizing the thermal properties of the Target and Earth.

4.1. Target radiative model

After establishing a simplified geometrical model of the Target, a finite volume thermal simulation is performed to compute the temperature field under illumination and eclipse conditions. To generalize the final data-set, three different material combinations are defined.

4.2. Earth radiative model

Rather than implementing an entirely new analytical framework to describe the thermal behaviour of the Earth and its atmosphere, numerical daily measurements from the Synoptic Radiative Fluxes and Clouds (SYN) library of the CERES database are leveraged to reconstruct the all-sky TOA temperature fluxes. Although the database provides measurements at a 1° resolution, considering the Earth's dimensions, this coarse mesh would result in an image with extremely low resolution. Hence, a mesh refinement at 0.1° resolution is imposed, and the final temperatures for each mesh location are recovered through an interpolation process. The recovered temperature field as seen from the space is reported in Figure 2.

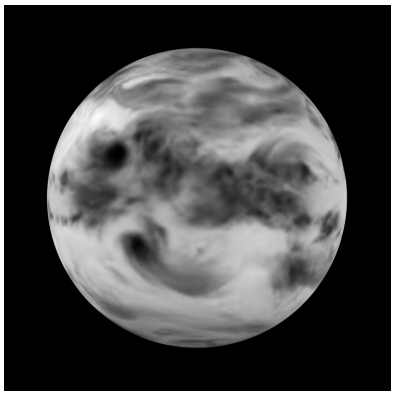

Figure 2: Earth's temperature field.

From the knowledge of the all-sky temperature, Eq.1 is exploited to recover the radiation reaching the detector of the thermal camera, and, depending on the selected camera mode, the digital output is computed according to the presented formulation.

4.3. Image merging

To ensure a coherent final representation, the foreground and background images are rendered according to a unified radiance scale, determined on the basis of the selected camera mode. Subsequently, a merging operation is performed to overlay the Target representation onto the Earth image, and Eqs.(2) and (5) are employed to compute the overall digital output corresponding to the observed scene. Note that for a correct image fusion between foreground and background, the Target representation is generated with a transparent background. In Figure 3, two exam-

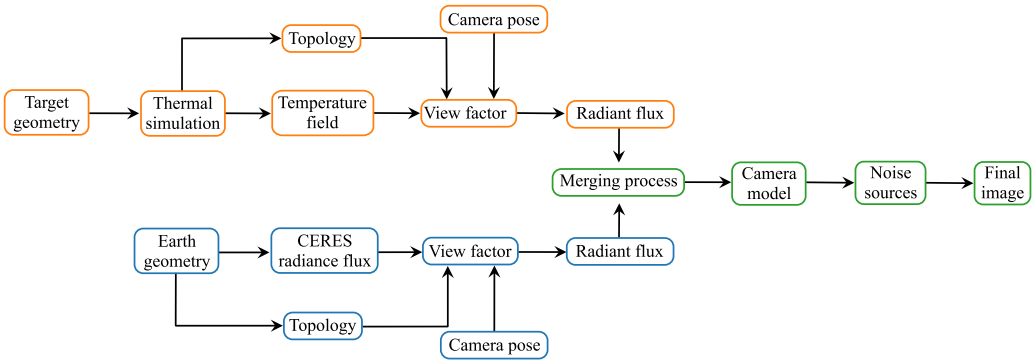

Figure 4: Rendering workflow sequence.

ples of TIR images rendered under radiometry and detection mode, respectively, are presented.

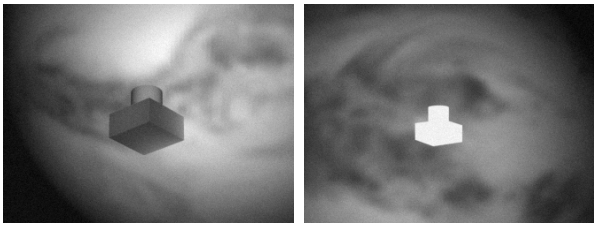

(a) Radiometry mode. (b) Detection mode.

Figure 3: Examples of noisy TIR images.

The final data-set generated with the proposed pipeline consists of 24000 images, enclosing noiseless and noisy counterparts. These images are representative of various scenarios, including close (15 m−50 m) and far-range (340 m−440 m) approaches, illumination and shadow conditions, and different material combinations. Furthermore, the data-set encompasses outcomes derived from both radiometry and detection modes.

5. ROI detection

In the field of optical navigation, image processing techniques are fundamental in extracting scene information. In this context, the generated data-set is leveraged to assess the performance of SoTA object identification algorithms, with the focus on Region of Interest (ROI) detection in monocular thermal images. Due to temporal and power constraints, this thesis focuses on the evaluation of the performance of traditional methodologies: Otsu thresholding, adaptive thresholding, Weak Gradient Elimination (WGE) approach and Difference of Gaussian (DoG) blob detection.

5.1. Results

Following the tuning of the hyper-parameters to improve the performance of the individual techniques, the algorithms' performance is evaluated based on the Intersection over Union (IoU) score and computational time.

Radiometry Considering the close-range class of the data-set, the performance of Otsu and DoG methods are extremely influenced by the highly textured background, particularly when the Earth's radiation level is comparable to those emitted by the Target. Differently, gradient-based technique and dynamic threshold are able to filter out the disturbance of the Earth, yielding performance which is much closer to that observed with visible imagery, achieving mean IoU scores of 0.85 in approximately 2 ms. As demonstrated by Figure 5, this performance remain consistent also for varying camera-Target distance.

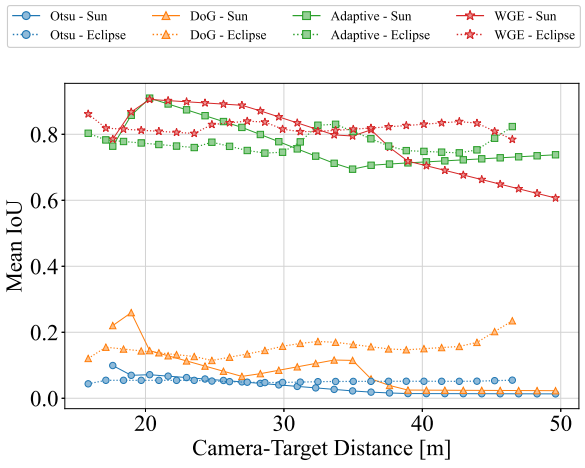

Figure 5: Average IoU in function of camera-Target distance in radiometry mode.

Yet, by moving the approach range towards the far-range, all methodologies show decreased performance due to the reduced size of the Target. Examples of detected ROI under radiometry mode are reported in Figure 6.

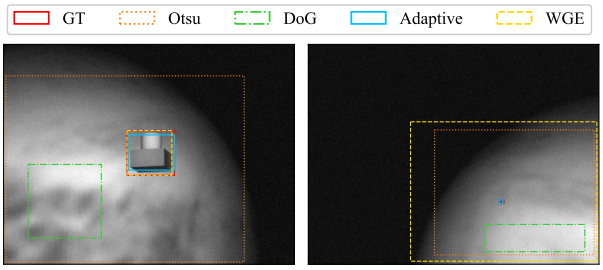

(a) Close-range. (b) Far-range.

Figure 6: ROI detected in radiometry mode.

Detection With reference to the close-range images, all approaches show improved performance with respect to the radiometry case. Being the Target represented by a plain saturated area, global thresholding and blob detector are eased in the detection process, resulting in higher IoU scores and reduced computational time. The outcomes are further increased when wider radiance scale intervals are considered, as the Earth presence is gradually removed from the image. Specifically, by imposing the upper limit of the scale as ten times the Earth's radiation, the Earth becomes almost invisible, leading to maximum detection performance. Similarly to the radiometry case, despite the Target being more distinguishable, its limited pixel coverage in far-range reduces the performance of all methods. Additionally, in this last scenario, DoG reaches a null average IoU, corresponding to undetected Target. Examples of extracted ROI under detection mode are reported in Figure 7, both for close and far approaches.

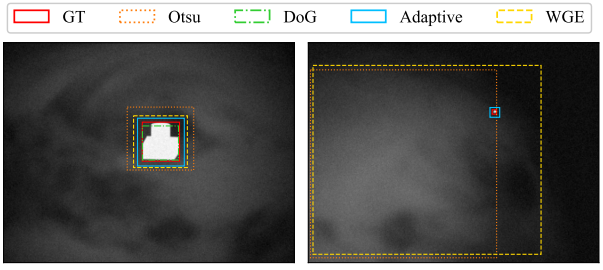

(a) Close-range. (b) Far-range.

Figure 7: ROI detected in detection mode.

6. Feature extraction

After extracting the most salient region in the image, the corresponding cropped portion of the frame is processed to recover the location of a predefined array of landmarks. To effectively fulfill navigation purposes, feature extractors shall be robust to scale and rotation variations. Hence, the chosen SoTA methodologies for evaluation are Harris corner detector and the gradient-based Oriented FAST and Rotated BRIEF (ORB) method [6]. Additionally, since the keypoints detected by ORB are prone to clustering, ORB with Density-Based Spatial Clustering of Application with Noise (DBSCAN) method is also evaluated.

6.1. Results

The implemented methodologies are evaluated on the basis of the Object Keypoint Similarity (OKS) and the Percentage of Detected Keypoints (PDK), where the latter metric is related to the number of correctly detected features. To achieve meaningful results, only the images generated under close-range radiometry mode, characterized by a more uniform radiance distribution, are considered for keypoint extraction tasks, as those generated in detection mode represent the Target as a completely saturated white region.

The performance of the tested methodologies is strictly related to the thermal properties of the material selected. If the spacecraft is characterized by a large portion of low emissivity material, such region will be displayed as a low-contrast area, hence the three algorithms are challenged in the localization process. To cope with this limitation, the Contrast Limited Adaptive Histogram Equalization (CLAHE) technique proves to increase the detection capabilities by enhancing the contrast of the image around the geometrical corners of the Target. As highlighted in Figure 8, the point A, which remains undetected when the original image is considered, is instead correctly detected when CLAHE algorithm is introduced.

Given the intrinsic nature of both ORB and Harris detector, they lack the capability of localizing non-corner like features. Hence, the Ground Truth (GT) landmark selected on the top face of the cylinder is recovered retrospectively in each frame in function of other detected features.

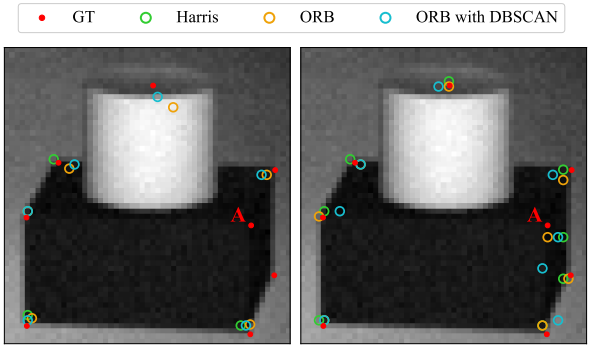

(a) Original image. (b) Equalized image.

Figure 8: Keypoint detected.

7. Conclusions

This thesis focuses on the development of an image processing pipeline for vision-based navigation tasks using monocular thermal imaging. This work underlines the importance of the definition of a physical model for the observed scene and its response to environmental changes, especially concerning the Earth and its atmosphere. This step enables the correlation among radiance values in both foreground and background, ensuring coherence in the final representation. To link the observed radiation field to the final pixel value, a model of the thermal sensor is introduced, together with a characteristic 2D noise map to enhance realism. The images generated with the presented pipeline prove effective for post-processing: while radiometry mode images are suitable for both ROI and feature extraction, granting results close to visible imagery, detection mode representations exclusively aid ROI detection. In general, it is proved that the detection accuracy of the Target varies with the material selected, detection range, and illumination conditions, where additional challenges are imposed by the presence of the Earth. Indeed, low emissivity regions affect the performance of feature extractors, partially addressed by the introduction of image enhancement algorithms.

7.1. Future work

Given the relevance of autonomous vision-based navigation, and the growing interest in the use of thermal sensors, this work represents promising starting results for future developments. Hence, some potential future development might be:

- Validate the generated data-set of images with the outputs of a real thermal sensor, with the focus on verifying the assumption of the inclusion of a compensatory factor contingent upon the camera-Target distance;
- The current use of traditional computer vision (CV) methods in post-processing is here acknowledged, but the potential of machine learning algorithms, especially for non-corner landmark identification, is suggested.
- From the knowledge of the derived 2D coordinates serves as potential input for the reconstruction of the 3D pose of the Target using monocular thermal imaging.

References

[1] J. Tao, Y. Cao, M. Ding, and Z. Zhang. "Visible and Infrared Image Fusion-Based Image Quality Enhancement with Applications to Space Debris On-Orbit Surveillance". *International Journal of Aerospace Engineering*, 2022.

[2] R. Peyrou-Lauga. "An enhanced Earth InfraRed flux and Albedo model based on real data". In *51st International Conference on Environmental Systems*, 2022.

[3] NASA. CERES project, 1997. URL `https://ceres.larc.nasa.gov/`. Accessed: 2023-05-17.

[4] T. Arai, T. Nakamura, S. Tanaka, H. Demura, Y. Ogawa, N. Sakatani, Y. Horikawa, H. Senshu, T. Fukuhara, and T. Okada. "Thermal Imaging Performance of TIR Onboard the Hayabusa2 Spacecraft". *Space Science Reviews*, 208, 2017.

[5] Y. Gao, H. Chen, Y. Xu, X. Sun, and B. Chang. "Noise research of microbolometer array under temperature environment". In *International Symposium on Photoelectronic Detection and Imaging 2011: Advances in Infrared Imaging and Applications*, volume 8193, 2011.

[6] X. Xiong and B. Choi. Comparative Analysis of Detection Algorithms for Corner and Blob Features in Image Processing. *International Journal of Fuzzy Logic and Intelligent Systems*, 13, 2013.